16th Australasian Wind Engineering Society Workshop
Brisbane, Australia
18-19 July, 2013

Wind tunnel investigation of the wake behind two porous high-rise buildings with the same porosity

S. Cochard[1], E. Paterna[2], P. Moonen[3] and J. Carmeliet[2,3]

[1]School of Civil Engineering, Faculty of Engineering and IT
The University of Sydney, Sydney, NSW 2006, Australia

[2]Building Science and Technology Laboratory
Empa - Swiss Federal Laboratories for Materials Science and Technology, Dubendorf, Switzerland

[3]Chair of Building Physics, Department of Architecture
ETH-Zürich, Zurich, Switzerland

Abstract

The velocity field in the wake of two porous high-rise buildings was measured and compared with the wake behind a similar solid building. The recirculation zone, which is typical of the wake of a high-rise building, is pushed downstream by the airflow that goes through the porous buildings. The recirculation zone is weaker behind the porous buildings than behind the solid one. Even if both porous buildings have the same porosity, their wake is found to be different.

Introduction

In an effort to densify the urban space, recent architectural projects have proposed to build high-rise building with open floors creating de facto porous buildings. The latest example of porous buildings, to the authors best knowledge, was presented by the Rotterdam based architectural firm MVRDV and The Why Factory during MIPIM's (le Marché International des Professionnels de l'Immobilier) first edition of the Innovation Forum held last March in Cannes, France. The results of their ongoing research on "the design of skyscrapers and the potential of porosity as a European approach to urban density", was presented as scale models made of Lego® bricks[1]. In this paper, a wind tunnel study on the flow behind porous buildings is presented. Two high-rise building with the same porosity are compared with a solid building.

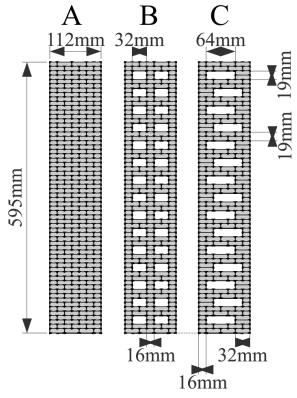

Figure 1: Sketch of the three configuration of Lego buildings. Each building is 62 Lego brick in height.

Methods

Wind tunnel tests were performed to study the flow around porous high-rise buildings. Ten buildings where built out of Lego bricks resulting, as some buildings were not symmetric, in fourteen different configurations. Particle Image Velocimetry (PIV) was used to measured the flow velocity in the wake of the buildings. In this paper, due to page constrains, three configurations are presented; one solid building (A) and two porous buildings (B and C). The two porous buildings have the same porosity.

All the models studied were hollow square cylinders with an outside width dimension W of 112 mm $\times$ 112 mm, a wall thickness T of 16 mm, and, a vertical height H of 595 mm. Figure 1 sketches the 3 configurations studied in this paper. Configuration A is the reference solid building with no openings, except for the roof. Configurations B and C are symmetric around the central axis with four identical façades. Both configurations B and C have the same porosity $\sigma = 0.27$, defined by the ratio of the surface opening to the total surface of the facade. All buildings were composed of 62 layers of Lego bricks, each Lego brick having a height of 9.6 mm (plus 1.6 mm for the interlock cylinders). Configurations B and C were built by making two solid layers of Lego topped by a two Lego brick height layer with openings, the pattern was reproduced 15 times and topped with an extra two solid layers of Lego bricks.

Figure 2: Photo of the three Lego buildings A, B and C.

The only difference between configurations B and C is the arrangement of each opening. Configuration B has two side-by-side openings of 32 mm $\times$ 19 mm with one column of 16 mm between them made of one 4 $\times$ 4 Lego brick. Configuration C has one opening of 64 mm $\times$ 19 mm where the extra 4 $\times$ 4 Lego brick is placed on alternating sides of the opening to guarantee the same opening area as configuration B. All three configura-

[1]http://archinect.com/news/article/66909344/mvrdv-builds-porous-city-exhibition-with-legos-in-cannes

tions are free from any obstruction in the central hollow space. Figure 2 shows the three Lego buildings A, B and C.

Wind-Tunnel Tests

The ETHZ/EMPA Atmospheric Boundary Layer Wind Tunnel (ABLWT), where the tests were carried out, is a close-loop wind tunnel with a cross section of 1.9 m$\times$ 1.3 m (width $\times$ height) and a fetch of 8 m. The maximum wind speed that can be generated in the test section is 25 m/s. The wind tunnel is equipped with a time-resolved stereo-PIV system (David and Gicquel, 2006; Felli et al, 2002; Prasad, 2000) which allowed the 3 components of the velocity field to be recorded on a planar region of interest (ROI) of 225 mm $\times$ 125 mm at a frequency of 600 Hz. The high-speed stereo-PIV system was composed of two 2016 x 2016 pixel cameras and one dual cavity Nd:YLF Laser with a maximum pulse energy of 30 mJ/pulse at 1 kHz. The two cameras were positioned on each side of the wind tunnel glass test section with a downward angle of $\sim 30^{\circ}$ (see Figure 3). Each camera was equipped with a Scheimpflug adapter to keep the ROI in focus.

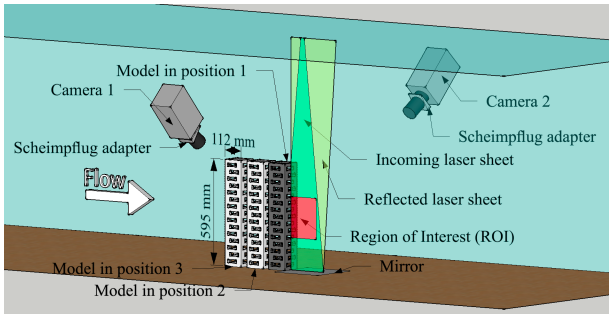

Figure 3: Sketch of the EMPA wind tunnel with the porous building C.

In this paper, by convention, the x-axis is the stream-wise direction, the y-axis is the cross-wise direction, and, the z-axis is the vertical direction. The coordinate system is fixed relative to the model, with; $z = 0$ on the tunnel floor, $y = 0$ in the symmetry plane of both the tunnel and the model, and, $x = 0$ attached to the downstream side of the model. (see Figure 3). The left and right sides of the building are defined as seen from downstream, so negative values of y define the left side of the model, while positive values of y define the right side.

Each model was placed in the test section with its axis of symmetry aligned with the y-axis. For each configuration, 8 tests were performed:

- three vertical PIV measurements were performed in the wake of the building by moving the building upstream and keeping the PIV setup fix relatively to the wind tunnel. Each building was moved upstream twice by a distance of 148 mm from position 1 to position 3 (see Figure 3). By moving the building upstream by 148 mm each time, the PIV measurements of the wake overlapped by 20 mm. The three ROIs were then combined to give a velocity field ranging from $x = 0$ mm to $x = 470$ mm and from $z = 185$ mm to $z = 410$ mm.
- one horizontal PIV measurement at mid-height of the model (z=147 mm) and covering a ROI ranging from $y = 60$ mm to $y = -170$ mm. The horizontal measurement plane was intentionally moved on one side of the model to record the free stream.
- for each PIV plane, one 1000-image set was grabbed at low frequency to ensure statistically independent results,
- for each PIV plane, one 2.6 s time-resolved PIV series was recorded at 600 Hz, resulting in 1560 images. Only the time average results are presented in this paper.

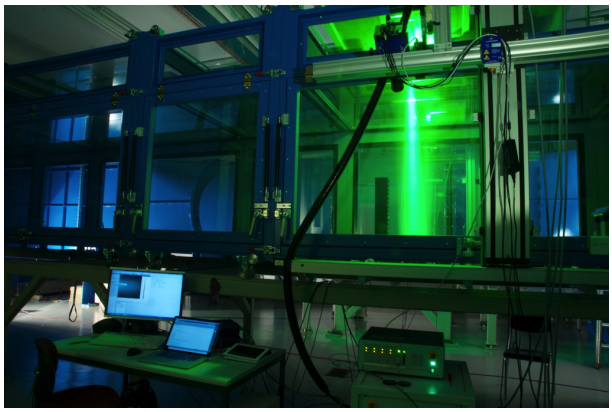

Figure 4: Photo taken during a test with the high-rise model in position 3.

All tests were performed at the same nominal velocity of 8 m/s. The ABLWT was, for this test campaign, not equipped with any roughness elements, spikes or trip boards, to minimise the turbulence level in the test section. The objective of this study was to study the influence of the porous building in a smooth flow and not to create atmospheric boundary conditions. Figure 5 shows the measured flow profile in the test section in blue and a best fit in red. The best fit function is given by:

$$\bar{u} = \begin{cases} \frac{u^*}{0.40} \cdot \ln\left(\frac{z+z_0}{z_o}\right) \text{ [m/s]}, & z < 150 \text{ mm} \\ 8 \text{ [m/s]} & z \geqslant 150 \text{ mm} \end{cases}$$

where z is the height above the wind tunnel floor in millimetres, $u^* = 1.1$ m/s is the friction velocity and $z_0 = 0.10$ mm is the roughness height. The turbulence intensity is below 1%.

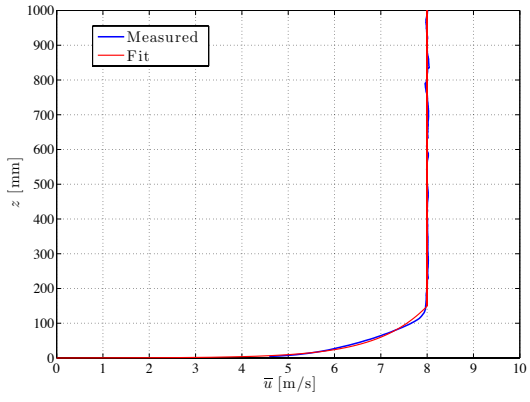

Figure 5: Test section velocity profile. In blue the measured profile and in red a double exponential best fit.

The two cameras were calibrated by means of a three-dimensional calibration plate and a further self-calibration

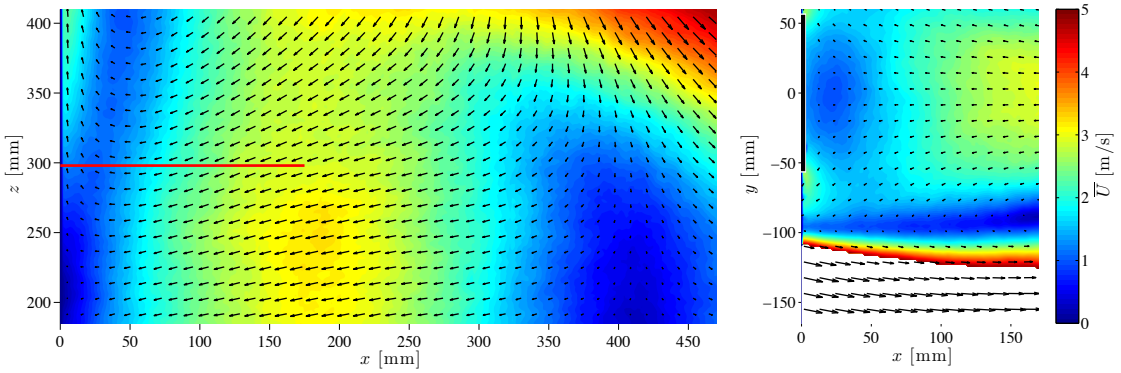

(a) configuration A

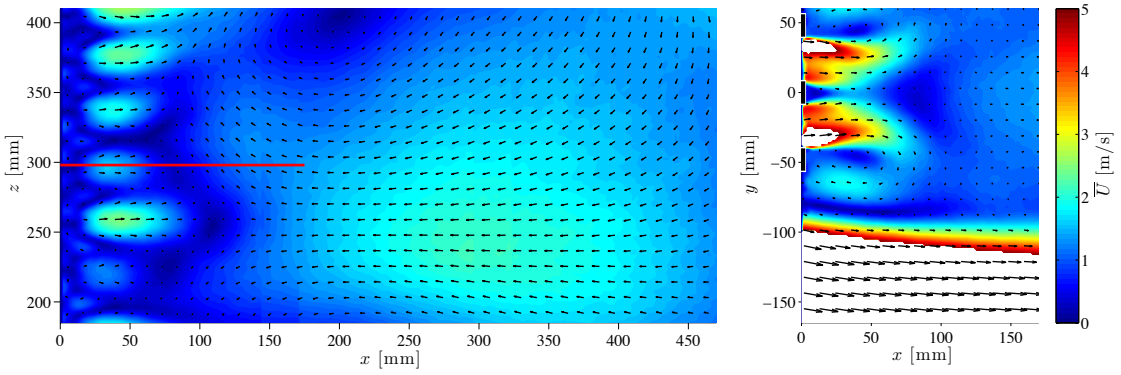

(b) configuration B

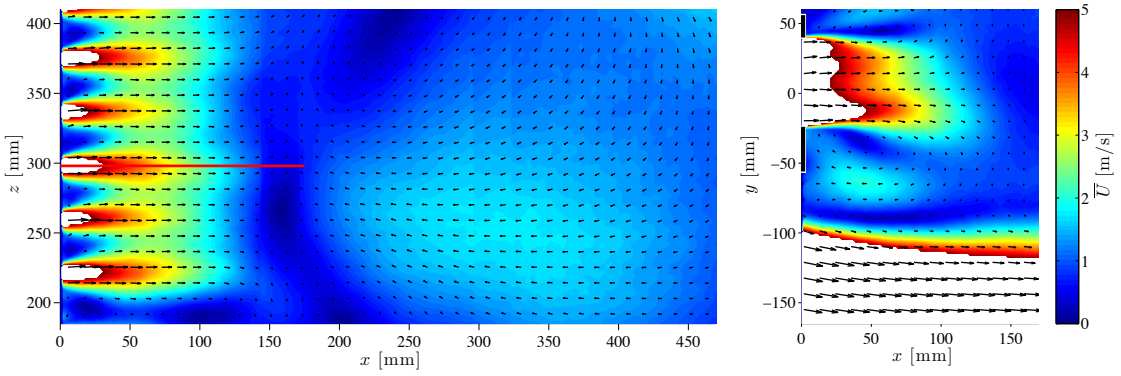

(c) configuration C

Figure 6: Time average of the velocity field in the wake of the model, (a) for configuration A, (b) configuration B, and, (c) configuration C. The left hand side graphics are the vertical velocity field at $y = 0$ mm, while the ones on the right are the horizontal velocity fields at $z = 147$ mm. The horizontal red lines on left graphics represent the horizontal ROI shown in on the right graphics. On the right hand side graphics the bulling back wall is schematised with black lines.

(Wieneke, 2005) was performed to allow an improvement of the camera mapping functions thus increasing the accuracy of the stereoscopic vector fields. The images were pre-processed first applying a background subtraction to improve the signal quality in presence of laser reflection. The images were then cross-correlated via a standard Fast Fourier Transform (FFT) algorithm and a multi-grid analysis with three passes and two refinement steps. The initial and final interrogation windows were set to 64 and 32 pixels respectively, both with 50% overlap, thus producing a spatial resolution of 3.2 mm. The vector fields were validated employing a threshold based on signal-to-noise ratio and a median filter.

Results

The time averaged velocity fields for the 3 configurations are presented in Figure 6. The velocity fields on the left hand side are the three combined velocity fields from the three vertical ROIs, while the velocity fields on the right hand side were computed from measurements made on the horizontal ROI. To ease the comparison, the six graphs use the same colour scale to plot

the average velocity magnitude $\bar{U} = \sqrt{(\bar{u}^2 + \bar{v}^2 + \bar{w}^2)}$. Velocities above 5 m/s are therefore in white, as outside the colour range. The vectors represent the velocity field (u,w) and (u,v) for the vertical (x,z) and horizontal (x,y) ROI respectively. To facilitate the interpretation of results, only one fiftieth of the vectors is plotted.

The flow behind building A (Figure 6(a)) shows a strong recirculation, as expected. The size of the recirculation zone downstream of the model, where the flow is moving back upstream, is approximately 2/3 of the model height H and displays velocity above 3 m/s. The centre of rotation of the recirculation zone is close to the building back wall (x=50 mm) and above the combined ROI. The flow along the building back wall is upward above $z = 220$ mm and downward below it. The flow separates at the upstream corners of the building (see Figure 6, right), does not reattach on the side walls and has values of 9 m/s, which is outside the colour range of the graphics and therefore in white.

Configuration B (Figure 6(b)) shows a larger recirculation zone than configuration A. The recirculation zone is pushed downstream by the flow that passes through the the building and is weaker, as can be seen by the lower upstream velocity which is approximately half of that found in configuration A. The combined ROIs do not cover the full length of the recirculation zone. At $x = 450$ mm the flow is mainly downward with a slight (~ 0.1 m/s) component toward the building. The flow that passes through the building exits the model by the downstream openings as 15×2 jets. The flow velocity in a jet is above 6 m/s. The vertical ROI does not record the jet velocity, as it is on the axis of symmetry of the building, which is, in this configuration, behind the 4×4 Lego bricks that separates the two openings (see Figure 3). The horizontal ROI, on the contrary, is located at $z = H/2$, and records the maximum velocity of the jet behind the openings. A careful analysis of the flow behind the jet on the horizontal ROI shows two horizontal recirculation zones, one for each jet. The two jets recorded display an upward velocity w above 0.5 m/s. The recirculation flow in the wake has a velocity toward the building that reaches values above 2.0 m/s. The vortex centre of the recirculation zone is positioned further downstream of the building than in configuration A, approximately 200 mm away front the back wall of the model and at $z = 410$ mm. The upstream flow, which was going up the building back wall in configuration A, has been replaced by the flow that passes through the building and therefore no stagnation point exists on the backward facade.

Configuration C (Figure 6(c)) displays the same trends as configuration B; the building wake is pushed further downstream and is weaker than in configuration A. In fact, the recirculation zone in configuration C has been pushed further downstream with a further reduction in strength compared to configuration B. The 15 openings create 15 strong jets that push the recirculation zone ~ 170 mm away from the building. At $x \approx 170$ mm, an approximately vertical virtual line with velocity $u = 0$ can be observed as on the back wall of configuration A. A similar bound can be observed in configuration B except that it is not a straight line but an S-curve. The jet on the horizontal ROI is asymmetric as is the opening, which ranges from $y = -24$ mm to $y = +40$ mm (see Figure 3). The maximum velocity in the jet is close to the $y = -24$ mm end with values above 7 m/s, which is slightly slower that the 8 m/s of the free stream velocity. The jet recorded by the horizontal ROI blows slightly upward with a w-velocity of 0.5 m/s. As in configuration B, the jets generate two horizontal recirculations on its sides. Of the two recirculation zones generated by the mid-height jet, the one on the left hand side of the building is the strongest. As in configuration A, the free stream that goes above the model supplies energy to the recirculation zone. The centre of rotation of the wake recirculation is at $y = 210$ mm and $z = 400$ mm.

Discussion

The wakes behind both porous buildings display the same characteristics than for the solid building (configuration A), but are situated further downstream from the building and with weaker strength. For all three configurations, the near field wake consist of a recirculation zone, which, in Figure 6, turns clockwise; in configuration A, the recirculation zone is attached to the building while in configurations B and C it is translated downstream by 100 mm and 170 mm respectively. The strength of the recirculation zone is also weaker in configuration C than in configuration B, with respective maximum backward velocities of 1.5 m/s and 2.5 m/s. The centre of the vortex, which is ~ 50 mm away from the model in configuration A, is moved to 210 mm and 250 mm for configuration B and C respectively.

Even though both porous models have the same porosity, the wake behind them is different and depends on the particular opening geomerties.. Configuration C displays a stronger flow going thought the building than configuration B; one opening allows more flow through the model than two openings. The maximum velocity in the symmetry plane of the building is 2.5 m/s in configuration B, compared to above 7m/s in configuration C.

Conclusion and future work

The velocity field in the wake of two similar porous buildings were measured at the EMPA/ETHZ atmospheric boundary layer wind tunnel, using a stereo-PIV system, and compared to a solid building. The flow behind the porous building is similar in the sense that they both push the recirculation zone of the wake further downstream than in the case of the solid building. But, even if both buildings present the same porosity, the flow behind them is different, due to the ways the opening are arranged. Configuration B has a 30 openings, while configuration C has 15 opening with the same open area. In configuration C the mass flux thought the model is bigger and produces stronger jets thought the back wall. These jets push the recirculation zone of the wake away front the building façades.

To fully understand the effect of the porosity of the building, more configurations need to be studied. In this paper only three configurations have been investigated of the fourteen that have been acquired. Future work consists in the analysis of all of the configurations and, if needed, more configurations will be tested. In addition, a CFD analysis to compliment the experimental investigation will be carried out.

*

References

David L, Gicquel P (2006) Evolutions de la technique PIV à travers quelques conférences internationales de 2000 à aujourd'hui. In: Congrès Francophone de Techniques Laser, CFTL, Toulouse, France

Felli M, Pereira F, Calcagno G, Felice FD (2002) Application of stereo-PIV: Propeller wake analysis in a large circulating water channel. In: 11th Int. Symp. on Applications of Laser Techniques to Fluid Mechanics, Lisbon, Portugal

Prasad AK (2000) Stereoscopic particle image velocimetry. Experiments in Fluids 29(2):103–116

Wieneke B (2005) Stereo-piv using self-calibration on particle images. Experiments in Fluids 39(2):267–280